Imaging of Micromotion Targets With Rotating Parts Based on Empirical-Mode Decomposition

Xueru Bai, Mengdao Xing, *Associate Member, IEEE*, Feng Zhou, Guangyue Lu, and Zheng Bao, *Senior Member, IEEE*

Abstract—For micromotion targets with rotating parts, the inverse synthetic-aperture-radar image of the main body may be shadowed by the micro-Doppler. To solve this problem, this paper proposes an imaging algorithm based on the complex-valued empirical-mode decomposition. First, the radar echoes are decomposed into a series of complex-valued intrinsic-mode functions (IMFs). Then, the IMFs from the rotating parts and those from the main body are separated according to the characteristics of their zero-crossings. Finally, the well-focused imaging of the main body via traditional imaging algorithm and the accurate parameter estimation of the rotating part can be obtained. Both the imaging results for the simulated and measured data are given to verify the validity of the proposed algorithm.

Index Terms—Empirical-mode decomposition (EMD), inverse synthetic aperture radar (ISAR), micro-Doppler (m-D).

I. INTRODUCTION

WHEN A TARGET moves along the radar line of sight with a constant speed, the carrier frequency of its returned signals will be shifted, which is known as the Doppler phenomenon. For monostatic radar, the Doppler frequency induced by target radial velocity v_r can be expressed as $f_d = 2v_r/\lambda$. Often, the imaging target or some structures on the target are vibrating or rotating in addition to the target's bulk movement. These mechanical vibrations or rotations are referred to as micromotion dynamics. The target micromotion may introduce additional time-varying frequency modulations on the radar echoes and generate sidebands about the Doppler frequency induced by the main body. This is known as micro-Doppler (m-D) [1]–[4].

In inverse synthetic-aperture-radar (ISAR) imaging, the target can be viewed as a turntable model after the translational motion compensation, which includes range alignment and autofocusing. The rigid body that rotates a small angle uniformly during the imaging time has a constant Doppler fre-

quency. Therefore, the well-focused image can be obtained by the range-Doppler (RD) algorithm. For a micromotion target, however, its m-D induced by the vibrating or rotating part is a time-varying function. In such situation, the ISAR image of the main body may be shadowed, particularly when the m-D interference is emphatic. This would bring great difficulties to the image interpretation and feature extraction for both the main body and the rotating parts. Consequently, m-D extraction and mitigation is important in ISAR imaging for such targets, and there has been increasing attention in this study in resent years.

Several m-D feature-extraction algorithms in the literatures have been proposed [4]–[9]. In [4]–[7], high-resolution joint time–frequency algorithms incorporated with order statistics and wavelet transforms are developed for m-D feature extraction, and in [8], the radar signal is parameterized into a set of chirplet functions, and the m-D signal is extracted by chirp-rate thresholding. Recently, Hough and extended Hough transforms are used for m-D extraction [9]. In given conditions, these algorithms have achieved satisfying results. Since the micromotion of aerial targets is mainly induced by rotating structures, such as helicopter blades, in-flight aircraft rotors, etc., this paper focuses on the m-D separation for the main-body imaging of aerial micromotion targets with rotating parts.

In 1998, Huang *et al.* [10] proposed the empirical-mode-decomposition (EMD) algorithm. It adaptively decomposes the real-valued nonstationary signal into a small number of intrinsic-mode functions (IMFs). In addition, the time–frequency characteristic for each IMF is described by Hilbert transform. Later, the extension of the EMD algorithm, namely, the complex-valued EMD (CEMD) algorithm, can decompose complex-valued signals by zero-mean rotating-component extraction [13], [14]. This algorithm is more applicable to coherent radar imaging. In CEMD, components that rotate more rapidly are separated from the ones that rotate slowly, which may provide possibilities and merits for the m-D separation. In this paper, we utilize the CEMD algorithm to decompose the echo with m-D into a finite number of IMFs. Then, according to the characteristics of their zero-crossings, IMFs that corresponds to the main body and those that corresponds to the rotating part are separated. Finally, the well-focused imaging of the main body and the more accurate estimation of the rotation rate can be obtained. Although this paper focuses on the m-D separation induced by the rotating part, the proposed algorithm can be extended to m-D separation induced by the vibrating part easily.
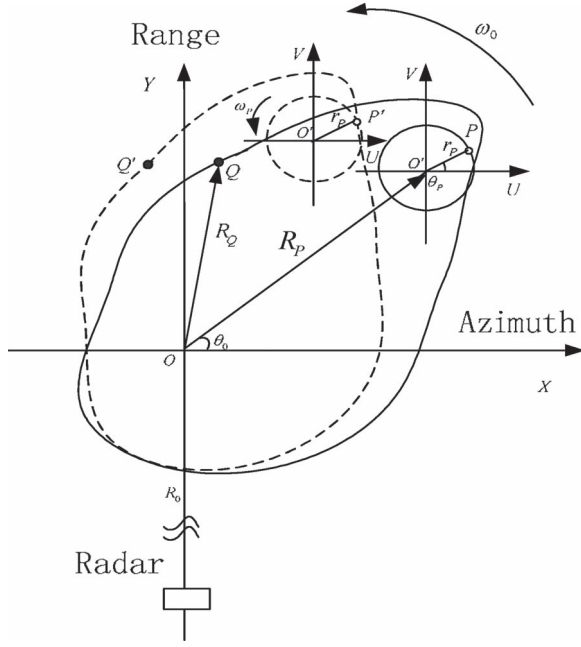
Fig. 1. Imaging geometry for micromotion targets with a rotating part.

II. SIGNAL MODEL FOR MICROMOTION TARGETS

Without loss of generality, this paper considers the imaging model of micromotion targets on the 2-D imaging plane. In the following discussions, we have the following assumptions.

1) Point-scattering model can be satisfied, i.e., the radar echo is assumed to be a sum of single-scattering objects.
2) The 2-D imaging plane is unchanged during the imaging time.
3) Almost no range migration exists among the scatterers from the main body.

The imaging geometry for a micromotion target is shown in Fig. 1, where the translational motion has been compensated, and the target has been converted into a turntable model. In this figure, XOY denotes the imaging plane, and $P(x_P, y_P)$ and $Q(x_Q, y_Q)$ denote the scatterer from the rotating parts and the main body, respectively. Their corresponding rotating radius are r_P and R_Q, respectively. Scatterer Q rotates uniformly around imaging center O, with the angular velocity to be ω_0 and the initial angle to be θ_0. Scatterer P rotates quickly around O', with the angular frequency to be ω_P and the initial phase to be θ_P. The dotted lines indicate the imaging geometry after a small angle rotation of the main body.

Usually, ISAR targets are relatively small. To obtain high range-resolution and reduce the effective bandwidth, the linear-frequency-modulated (LFM, i.e., chirp) waveform is adopted, and the dechirp technique (i.e., stretching) is employed. The waveform for the transmitted signal in the fast- and slow-time domain can be expressed as

$$s(\hat{t}, t_m) = a_{T_P}(\hat{t}) \exp\left(j2\pi\left(f_c t + \frac{1}{2}\gamma\hat{t}^2\right)\right) \quad (1)$$

where $a_{T_P}(\hat{t}) = \begin{cases} 1, & |\hat{t}| \leq T_P/2 \\ 0, & |\hat{t}| > T_P/2 \end{cases}$ denotes the window function and f_c, T_p, and γ are the carrier frequency, the pulsewidth,

and chirp rate, respectively. Let the reference point be the imaging center O, then the radar returns after dechirping can be expressed as

$$s_R(\hat{t}, t_m) = \sigma a_{T_P}(\hat{t}) \exp\left(-j\frac{4\pi}{c}\gamma\hat{t}R_\Delta(t_m)\right)$$
$$\times \exp\left(-j\frac{4\pi}{\lambda}R_\Delta(t_m)\right) \quad (2)$$

where σ, c, and λ denote the backscatterering coefficient, the speed of light, and the wave length, respectively. $R_\Delta(t_m)$ is the instantaneous range between the scatterer and imaging center. After range compression in the fast-time domain, (2) becomes

$$s_1(\hat{f}, t_m) = A\text{sinc}\left(T_p\left(\hat{f} + 2\frac{\gamma}{c}R_\Delta(t_m)\right)\right)$$
$$\times \exp\left(-j\frac{4\pi}{\lambda}R_\Delta(t_m)\right) \quad (3)$$

where $A = \sigma T_P$ denotes the signal amplitude. From Fig. 1, it can be found that the distance between scatterer Q and the reference point O satisfies

$$R_{\Delta Q}(t_m) = R_Q \sin(\omega_0 t_m + \theta_0). \quad (4)$$

Ignoring the initial phase and using the small accumulation angle assumption, the Doppler frequency of the main body is

$$f_{dQ} = \frac{2}{\lambda}\frac{\mathrm{d}\left(x_Q \sin(\omega_0 t_m) + y_Q \cos(\omega_0 t_m)\right)}{\mathrm{d}t_m} \approx \frac{2\omega_0}{\lambda}x_Q \quad (5)$$

where $x_Q = R_Q \cos\theta_0$ and $y_Q = R_Q \sin\theta_0$. Equation (5) shows that the scatterer from the main body possesses constant Doppler information approximately. Therefore, 2-D Fourier transform can be utilized directly on (2) to obtain the ISAR imaging, which is the RD imaging algorithm.

As shown in Fig. 1, $r_P \ll R_0$ and $R_P \ll R_0$, then the distance between scatterer P and the reference point O after dechirping satisfies

$$R_{\Delta P}(t_m) = R_P \sin(\omega_0 t_m + \theta_0) + r_P \sin(\omega_P t_m + \theta_P). \quad (6)$$

The corresponding Doppler information is

$$f'_{dP}(t_m) = \frac{2}{\lambda}\left(\omega_0 x_P + \omega_P r_P \cos(\omega_P t_m + \theta_P)\right) \quad (7)$$

where $x_P = R_P \cos\theta_0$. Ignoring the initial phase θ_P gives

$$f_{dP}(t_m) = \frac{2}{\lambda}\omega_0 x_P + \frac{2}{\lambda}\omega_P r_P \cos(\omega_P t_m)$$
$$= f_{dP0} + \frac{2}{\lambda}\omega_P r_P \cos(\omega_P t_m). \quad (8)$$

Therefore, the m-D of a rotating scatterer in addition to the target's bulk movement is a sinusoidal FM signal. Since the rotation rate of the main body is much smaller than that of the rotating part, its influence on the envelopes is negligible for
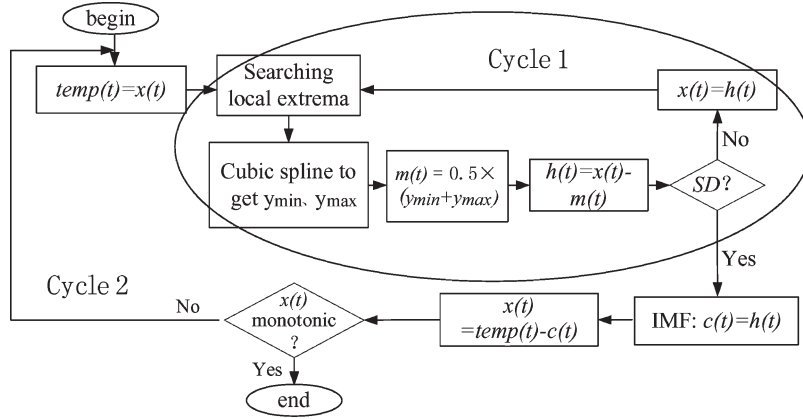
Fig. 2.　Diagram for real-valued EMD.

a small accumulation angle. Substituting (6) into (3), echoes from the rotating part after range compression are expressed as

$$
\begin{aligned}
s_{P1}(\hat{f}, t_m) &= A\,\mathrm{sinc}\left(T_P\left(\hat{f} + \frac{2\gamma}{c}r_P\sin(\omega_P t_m + \theta_P)\right)\right) \\
&\quad \times \left(-j2\pi f_{dP0}t_m - j\frac{4\pi}{\lambda}r_P\sin(\omega_P t_m + \theta_P)\right).
\end{aligned}
\tag{9}
$$

Suppose that no range migration occurs during the imaging time, then the approximation form of (9) satisfies

$$
s_{P2}(\hat{f}, t_m) = A'\exp\left(-j2\pi f_{dP0}t_m - jU\sin(\omega_P t_m)\right) \tag{10}
$$

where $A' = A\,\mathrm{sinc}(T_P(\hat{f} + (2\gamma/c)r_P\sin(\omega_P t_m)))$ and $U = 4\pi r_P/\lambda$. If we expand (10) using Bessel functions and carrying out the FT in the slow-time domain, we can obtain the spectrum of the m-D [4]

$$
\begin{aligned}
s_{P3}(\hat{f}, f_m) &= A'\mathcal{F}\left\{\sum_{l=-\infty}^{\infty} J_l(U)\exp\left(-j(2\pi f_{dP0} + l\omega_P)t_m\right)\right\} \\
&= A'\left\{J_0(U)\mathrm{sinc}\left(T_m(f_m - f_{dP0})\right)\right. \\
&\quad + J_1(U)\mathrm{sinc}\left(T_m(f_m - f_{dP0} - \omega_P)\right) \\
&\quad - J_1(U)\mathrm{sinc}\left(T_m(f_m - f_{dP0} + \omega_P)\right) \\
&\quad + J_2(U)\mathrm{sinc}\left(T_m(f_m - f_{dP0} - 2\omega_P)\right) \\
&\quad \left. - J_2(U)\mathrm{sinc}\left(T_m(f_m - f_{dP0} + 2\omega_P)\right) + \cdots\right\} \\
&\qquad\qquad\qquad\qquad\qquad\qquad l \in \mathbb{Z}
\end{aligned}
\tag{11}
$$

where T_m denotes the imaging time. The coefficient $J_l(U)$ is

$$
J_l(U) = \frac{1}{2\pi}\int_{-\pi}^{\pi}\exp\left(j(l\tau - U\sin\tau)\right)d\tau \tag{12}
$$

which satisfies
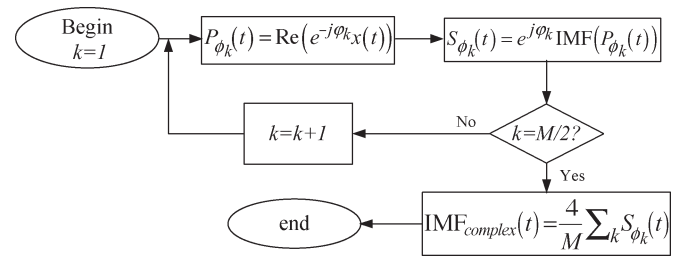
$$
J_{-l}(U) = (-1)^l J_l(U). \tag{13}
$$

Fig. 3.　Diagram for single IMF calculation using CEMD.

From (11), one can conclude that the m-D of a rotating scatterer is centered at f_{dP0} in the spectrum, with its sidebands equally spaced at multiples of ω_P. In addition, the bandwidth of the m-D is about $2U$, which is a function of wave length and rotation radius. Therefore, m-D may contaminate the image of the main body in the Doppler domain, particularly when it is emphatic. This conclusion also holds when range migration happens for the scatterers on the rotating part. Consequently, the m-D should be mitigated or eliminated to obtain a well-focused ISAR image of the main body.

III. m-D EXTRACTION BASED ON EMD ALGORITHM

A. Real-Valued EMD

In 1998, Huang *et al.* [10]–[12] introduced the EMD and Hilbert spectrum for nonlinear and nonstationary time-series analysis based on the local-characteristic time scale of the data. This algorithm consists of two parts. The first part is the EMD, which decomposes the real-valued signal into a finite number of IMFs. The second part is the calculation of Hilbert spectrum, in which the analytical signal for each IMF is obtained via Hilbert transform, and then, the corresponding instantaneous frequency is calculated according to the definition

$$
f_{\mathrm{inst}} = \frac{1}{2\pi}\frac{d\varphi(t)}{dt} \tag{14}
$$

where $\varphi(t)$ denotes the phase term of the analytical signal. Finally, 3-D distribution of energy–frequency–time, i.e., the Hilbert spectrum, can be reconstructed from the original signal. The essence of Hilbert–Huang transform is the EMD, which is realized using the *sifting process*. Being quite different from
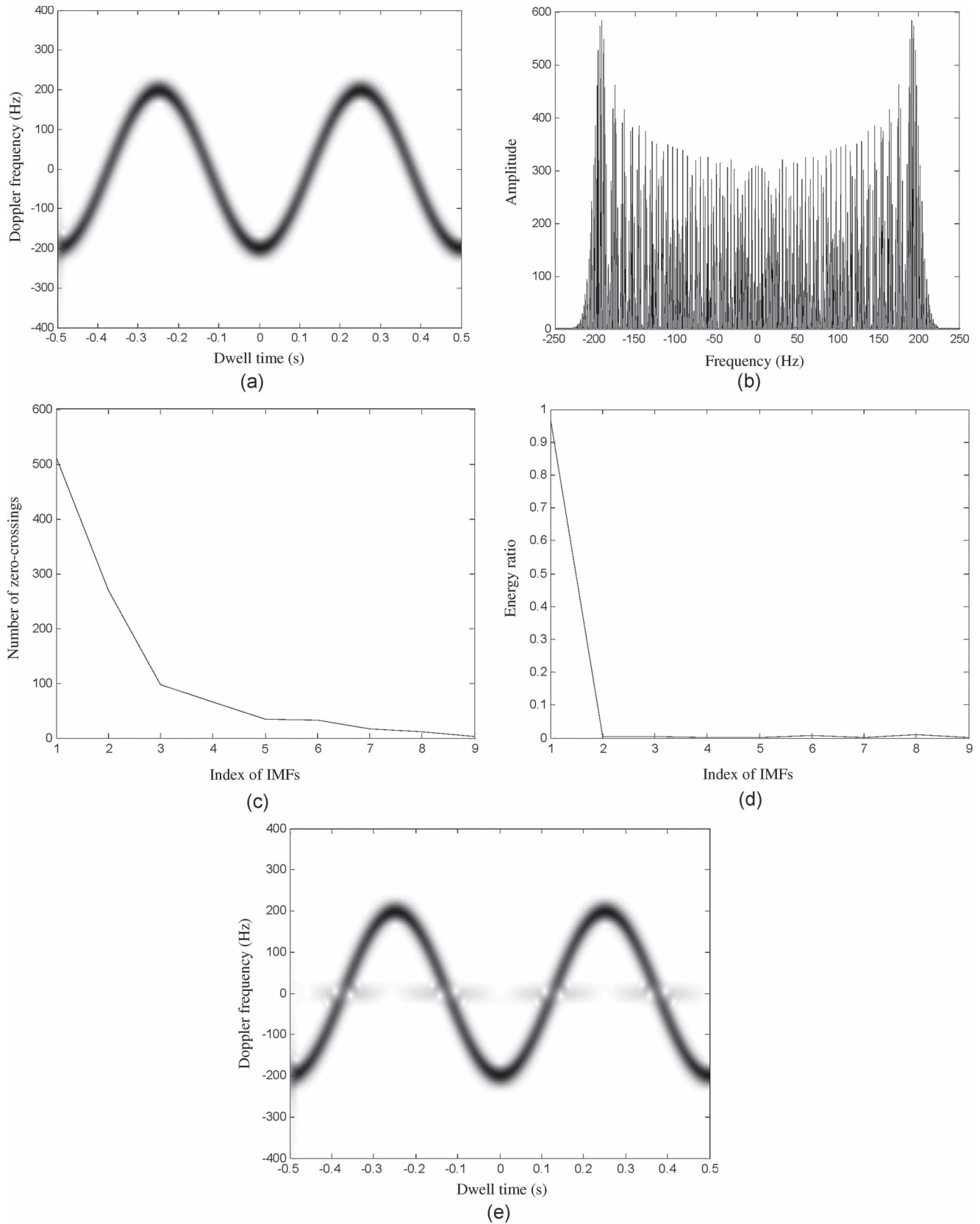
Fig. 4.   CEMD of the sinusoidal FM signal. (a) Spectrogram of the simulated signal. (b) Spectrum of the simulated signal. (c) Number of zero-crossings for each IMF. (d) Energy ratio for each IMF. (e) Spectrogram of the reconstructed signal.

the traditional global wave analysis, such as Fourier transform, etc., the EMD belongs to local wave analysis, which is based on signal local property. In addition, the obtained IMFs can be viewed as the basis functions for signal expansion. Therefore, this algorithm is adaptive and efficient. In addition, the decomposition is based on the direct extraction of the
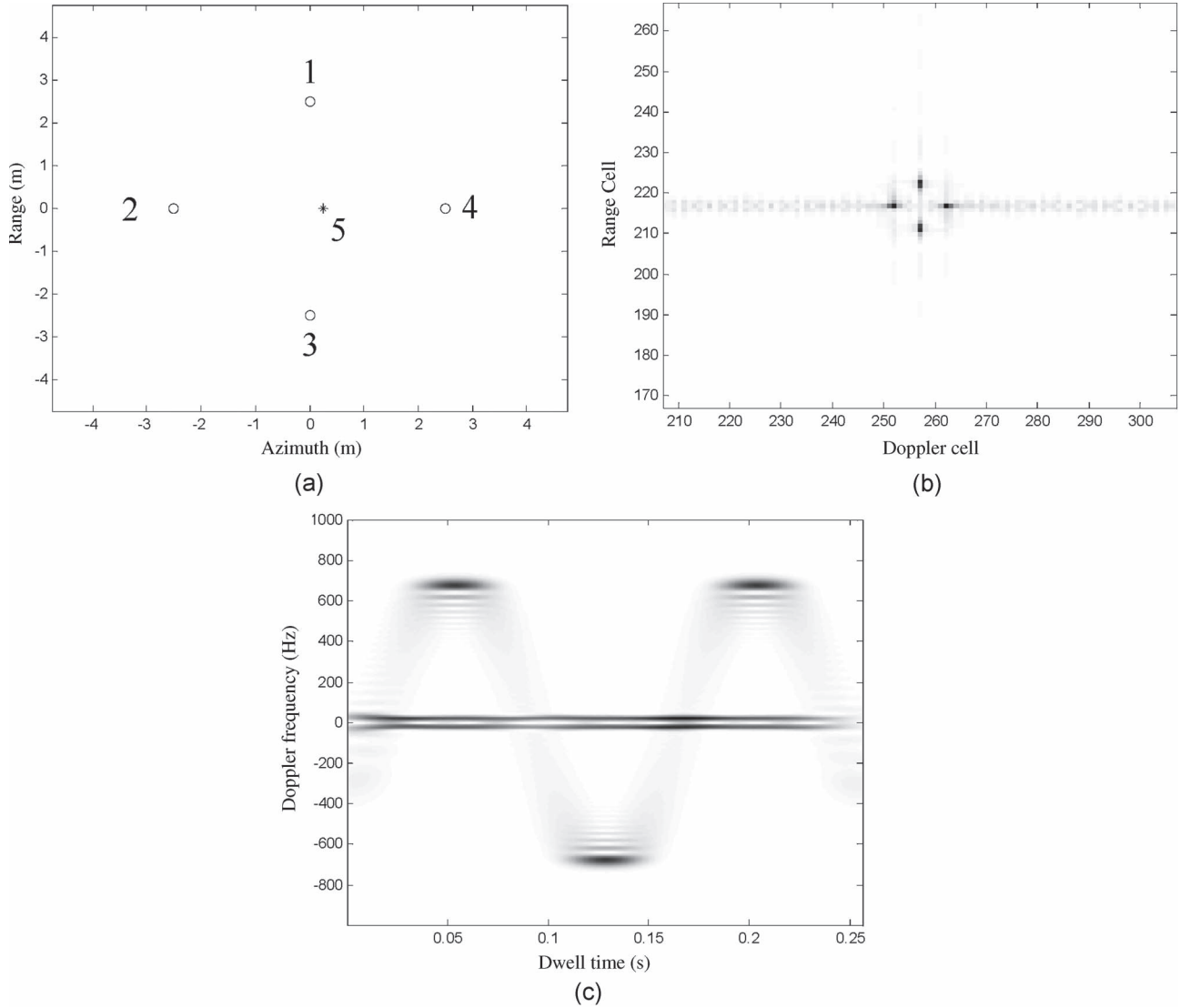
Fig. 5.   Image of the original echoes and spectrogram analysis. (a) Scatterer distribution. (b) Image of the raw data. (c) Spectrogram of range cell 217.

energy-associated various intrinsic time scales, which is the most important parameters of the system.

An IMF satisfies the following two conditions.

1) In the whole data set, the number of extrema and the number of zero-crossings must either equal or differ, at most, by one.
2) At any point, the mean value of the envelope defined by the local maxima and the envelope defined by the local minima is zero.

The diagram for real-valued EMD is shown in Fig. 2, in which $x(t)$ is the original signal. This algorithm includes two cycles. The first cycle is the *sifting process*, where $m(t)$ denotes the local mean of the envelopes defined by the local maxima and the local minima. In this cycle, the threshold SD is defined as

$$\text{SD} = \sum_{t=0}^{T} \left[\frac{\left| h_{i(k-1)}(t) - h_{ik}(t) \right|^2}{h_{i(k-1)}^2(t)} \right] \qquad (15)$$

where subscript i denotes the ith sifting process and k and $k-1$ denote the two adjacent intermediate results. To ensure

the physical sense of each IMF, the stop criterion for the sifting process is SD $\in [0.2, 0.3]$. If SD satisfies the presetted threshold, then $h(t)$ is designated as $c(t)$, i.e., an IMF. Then, subtract $c(t)$ from the original signal temp(t) and continue cycle two until $x(t)$ is monotonic. After EMD, signal $x(t)$ can be expressed as a summation of the n IMFs and a residue, i.e.,

$$x(t) = \sum_{i=1}^{n} c_i(t) + h(t). \qquad (16)$$

From the earlier analysis, it is noticed that the spectral region of supports of these IMFs varies from high to low gradually, since the new sifting process is based on the residue signal from the previous one. Therefore, the EMD decomposition is functioning as a filter bank with different frequency passbands. However, it is worth pointing out that the EMD does not correspond to a predetermined subband filtering. Instead, this algorithm is actually an adaptive time-variant filtering, based on the intrinsic characteristic of the data.
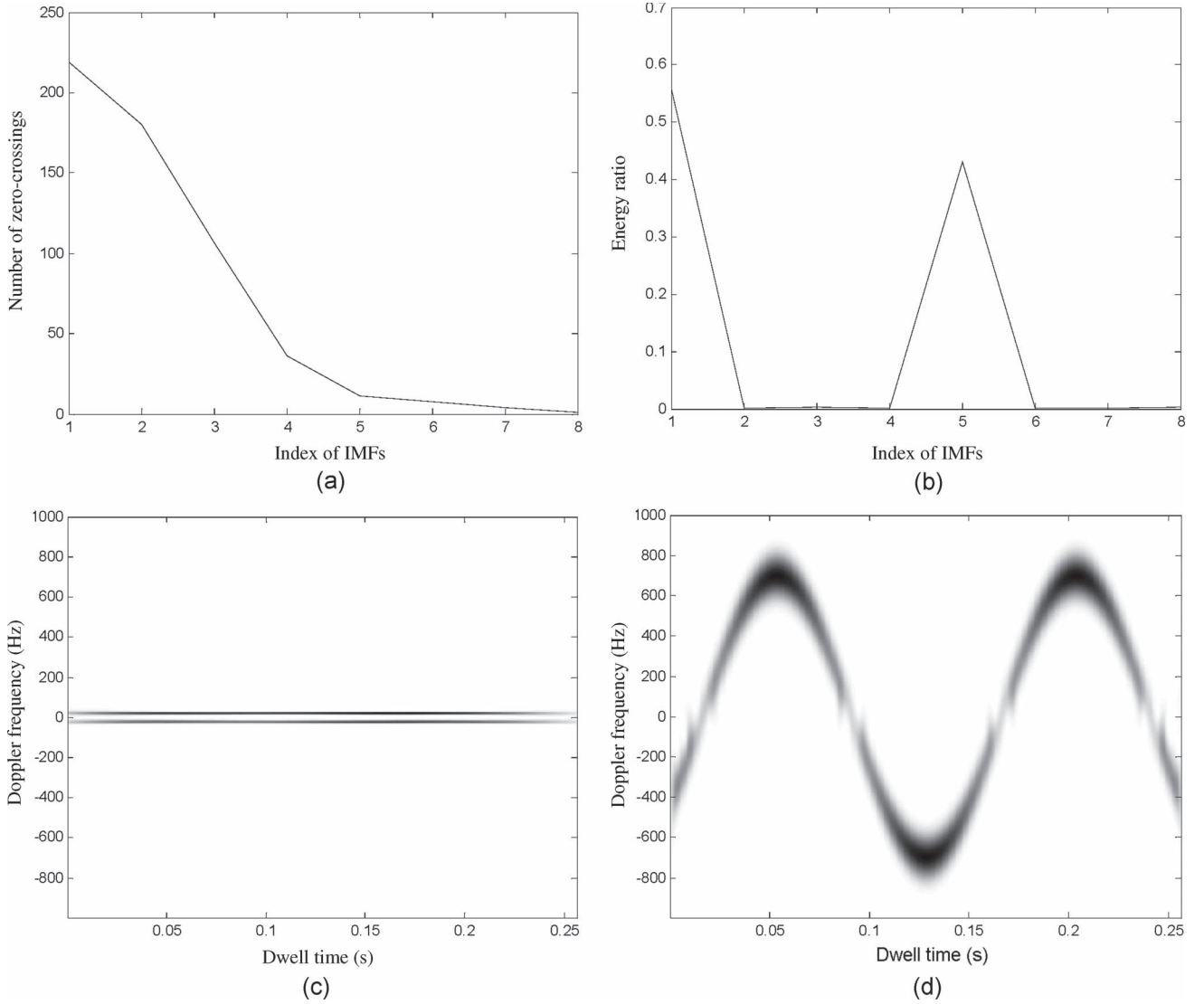
Fig. 6.   m-D separation via CEMD. (a) Number of zero-crossings for each IMF. (b) Energy ratio for each IMF. (c) Spectrogram for the main body. (d) Spectrogram for the rotating part.

B. CEMD

In most engineering environments, the quadrature-sampling technique is utilized in the receiver, and complex-valued signals with amplitude and phase information are generated. In radar-imaging area, signal coherency is particularly a necessity. However, the coherency will be destroyed in the real-valued EMD. Recently, Rilling *et al.* [14] presented two novel CEMD algorithms. The difference between EMD and CEMD is that the real-valued EMD attempts to extract zero-mean oscillation components while the CEMD extract the zero-mean rotating components. Therefore, the result of CEMD is a number of complex-valued IMFs, whose rotation vector varies from fast to slow.

In the CEMD algorithms, the mean of the 3-D envelope is defined as the center of the enclosing tube in specific directions, which are defined as $\exp(-jk\pi/M)$, $0 \leq k \leq M-1$. In this formula, M denotes the number of directions to be selected. In this paper, the mean of the maximum points in the specific directions is treated as the mean rotation vector. Then, the

CEMD algorithm can be regarded as a modified real-valued EMD. The diagram of this algorithm is shown in Fig. 3.

In Fig. 3, $\mathrm{Re}(\bullet)$ denotes the real part of a complex-valued signal, and IMF$(\bullet)$ is the IMF of the real-valued signal P_{φ_k}. If the number of directions is even, only IMFs from $M/2$ directions need to be calculated, considering the symmetry of directions.

C. m-D Extraction via CEMD

From (14), one can conclude that the m-D frequencies are multiples of ω_P and can be expressed as $f_{dP0} \pm n\omega_P$, $n = \pm 1$, $\pm 2, \pm 3, \ldots$. In addition, the Doppler frequency induced by the main body is relatively small for the small aerial targets, given small accumulation angle. Therefore, the frequencies of m-D signals are generally higher than those of the main body. Since different zero-mean rotating components reflect different modes of frequencies, the m-D signals can possibly be extracted, if the threshold value is properly selected.
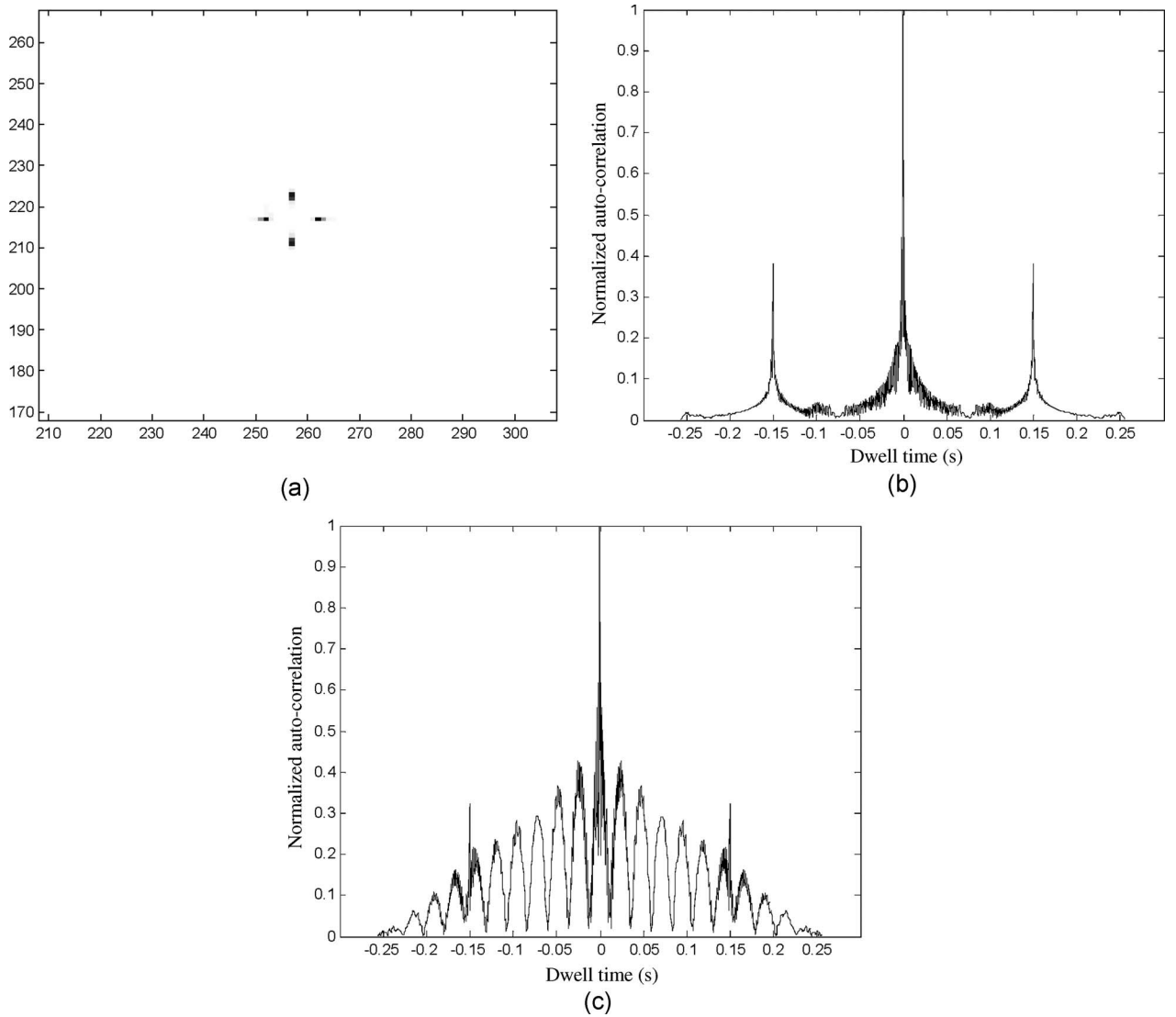
Fig. 7. m-D extraction and imaging for simulated data. (a) Image of the main body. (b) Normalized autocorrelation of m-D signals. (c) Normalized autocorrelation of raw data.

For an IMF, its average period T_{ave} can be defined by

$$T_{\mathrm{ave}} = N/N_{\mathrm{zero-crossing}} \qquad (17)$$

where N denotes the data length and $N_{\mathrm{zero-crossing}}$ is the number of zero-crossings.

When a sinusoidal FM signal (i.e., an m-D signal) is decomposed via CEMD, the obtained IMFs also includes rotating vectors varying from fast to slow. However, most part of the signal energy exists in the IMFs with shorter average period, while only a small part of the energy exists in IMFs with longer average period. Therefore, the threshold of zero-crossings is insensitive to the m-D extraction accuracy, which can guarantee the robustness of this method. Therefore, in this paper, the number of zero-crossings is selected as a threshold to realize m-D extraction.

Since both the EMD and CEMD techniques cannot be defined by any analytical formulation, the experimental data are utilized to explain the m-D extraction algorithm. Let the rotating frequency be 2 Hz and U be 100, the signal can be
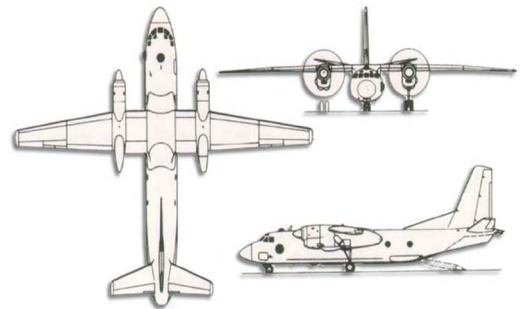

Fig. 8. Framework for AN-26 plane.

written as $x(t) = \exp(j100\sin(2\pi \times 2t))$. The data sampling rate is 2000 Hz. Fig. 4(a) shows the spectrogram of this signal, whose instantaneous frequency is a sinusoid. The peak value in this figure locates at 200 Hz, corresponds to the maximum instantaneous frequency. Fig. 4(b) shows the spectrum obtained via FT. The distance between adjacent lines is 2 Hz, which is consistent with (11). After CEMD, the original signal is
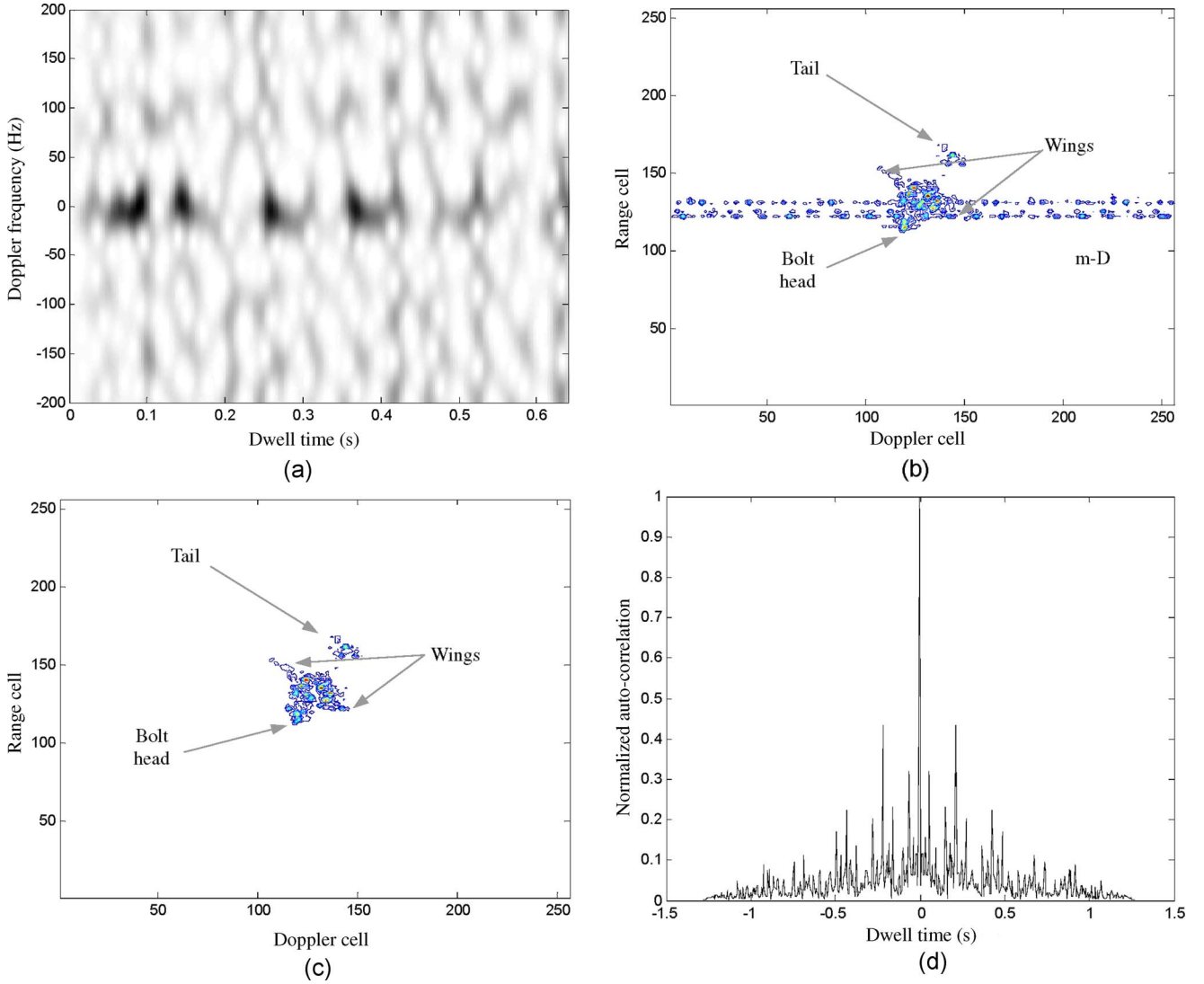
Fig. 9. Image for measured data. (a) Spectrogram for range cell 131. (b) Image of raw data. (c) Image of the main body. (d) Normalized autocorrelation of m-D in range cell 131.

decomposed into nine IMFs and a residue. The number of zero-crossings and the energy ratio for each IMF are shown in Fig. 4(c) and (d), respectively. From Fig. 4(c), one can see that the number of zero-crossings decreases rapidly. In addition, Fig. 4(d) shows that most energy (about 97%) of this sinusoidal FM signal lies in IMFs with short average period. Fig. 4(e) shows the spectrogram of the reconstructed signal via the first six IMFs, which is in good agreement with Fig. 4(a). This example indicates that the m-D signal actually corresponds to IMFs with short average period.

IV. SIMULATIONS

In this section, we verify the proposed algorithm using simulated data. Five scatterers are used in the simulation, with four of them representing the main body and one representing the rotating part. Fig. 5(a) shows the positions of the scatterers. Scatterer 5 rotates around $(0, 0)$ at a rate of 6.67 Hz, and its rotation radius is 0.25 m. The main body rotates about $1.84°$ over 512 pulses during the imaging time. The radar bandwidth

is 300 MHz, and the pulse repetition frequency is 2000 Hz. In addition, the backscattering coefficient of the rotating part is twice than that of the main body.

The echoes are generated using the point scattering model. Fig. 5(b) shows the resulted radar image of the raw data via the RD algorithm. As shown in the figure, the images of scatterers 2 and 4 are shadowed by the m-D interference from scatterer 5. Since the radar returns from the main body and the rotating part have different time–frequency characteristics, one can study them in the spectrogram domain. Taking range cell 217 that consists of echoes from scatterers 2, 4, and 5 as an example, and its spectrogram is shown in Fig. 5(c). In this figure, the two horizontal lines reflect two scatterers from the main body, and the blurred sinusoidal curve reflects the frequency characteristic of scatterer 5. Since the m-D signal is nonstationary, its time–frequency concentration is lower than the two straight lines from the main body.

Then, the echo is decomposed into eight IMFs via CEMD. The number of zero-crossings for each IMF is 219, 181, 110, 46, 37, 11, 8, and 3, respectively, as shown in Fig. 6(a). Since

the last five IMFs have much smaller zero-crossings than the other ones, it can be inferred that they contain responses from the main body. In addition, the energy ratio for each IMF is shown in Fig. 6(b). Two peaks appear in this figure; the first one reflects scatterer 5, while the second one reflects energy from scatterers 1, 2, 3, and 4. Based on the observation, the threshold value is selected to be 30. Then, the spectrograms for the main body and the rotating part are shown in Fig. 6(c) and (d), respectively. One can see that echoes from the main body with constant Doppler and the echo from rotating part with fast-changing Doppler frequency are separated.

In addition, the earlier algorithm can also be applied to other range cells with m-D. Finally, image of the main body is shown in Fig. 7(a), where the four scatterers are well focused. Fig. 7(b) shows the normalized autocorrelation for the extracted m-D in range cell 217. The rotation period is estimated to be 0.15 s from this figure. Therefore, the rotation frequency for the rotating part is 6.67 Hz. The normalized autocorrelation for the raw data is shown in Fig. 7(c), and the estimated rotation rate from this figure is 40 Hz. The comparison of these two estimations indicates that the extraction of m-D can improve the accuracy of parameter estimation for rotating parts.

V. IMAGING FOR THE MEASURED DATA

In this section, the algorithm mentioned earlier is applied to measured data of the AN-26 plane. As shown in Fig. 8, it is a turboprop applied to short-range transportation, with two turbos on each side of the airframe. The radar bandwidth is 400 MHz, and the PRF is 400 Hz.

Fig. 9(a) shows the spectrogram of the echo in range cell 131. One can observe that the Doppler of the main body exists around the zero frequency. In addition, the m-D occupies the whole spectrum due to the frequency modulation of turbo blades. Fig. 9(b) shows the ISAR image of the raw data by the RD algorithm. Two m-D bands occupy the whole Doppler spectrum, and the image of the main body is contaminated.

According to the proposed algorithm, we first apply CEMD to echoes in different range cells with m-D. The number of directions in the CEMD algorithm is set to be 128. Then, proper threshold value is selected for m-D separation, according to the characteristic of zero-crossings for each IMF. After that, IMFs containing m-D are extracted, while the remaining ones are employed to form an ISAR image of the main body.

Fig. 9(c) shows the contoured image of the main body. Compared with Fig. 9(b), the m-D interference is suppressed, and the wings are well focused. Fig. 9(d) shows the normalized autocorrelation coefficient for m-D in range cell 131, and the estimated rotation rate from Fig. 9(d) is 20 Hz.

VI. CONCLUSION

This paper proposes a new ISAR imaging algorithm for micromotion target with rotating parts based on CEMD. In this algorithm, we first decompose the echoes into a series of IMFs. Then, IMFs that contain the m-D are separated by zero-crossing thresholding. Finally, we can obtain the well-focused ISAR image of the main body and the more accurate estimation of rotation rate of the rotating part.

REFERENCES

[1] V. C. Chen, F. Li, S.-S. Ho *et al.*, "Analysis of micro-Doppler signatures," *Proc. Inst. Electr. Eng.—Radar Sonar Navig.*, vol. 150, no. 4, pp. 271–276, Aug. 2003.

[2] T. Sparr and B. Krane, "Micro-Doppler analysis of vibrating targets in SAR," *Proc. Inst. Electr. Eng.—Radar Sonar Navig.*, vol. 150, no. 4, pp. 277–283, Aug. 2003.

[3] V. C. Chen, "Spatial and temporal independent component analysis of micro-Doppler features," in *Proc. IEEE Int. Radar Conf.*, 2005, pp. 348–353.

[4] V. C. Chen, F. Li, S.-S. Ho *et al.*, "Micro-Doppler effect in radar: Phenomenon, model, and simulation study," *IEEE Trans. Aerosp. Electron. Syst.*, vol. 42, no. 1, pp. 2–21, Jan. 2006.

[5] V. C. Chen, "Analysis of radar micro-Doppler signature with time–frequency transform," in *Proc. 10th IEEE Workshop Statistical Signal Array Process.*, 2000, pp. 463–466.

[6] L. Stankovic, I. C Djurovi, T. Thayaparan *et al.*, "Separation of target rigid body and micro-Doppler effects in ISAR imaging," *IEEE Trans. Aerosp. Electron. Syst.*, vol. 42, no. 4, pp. 1496–1506, Oct. 2006.

[7] T. Thayaparan, S. Abrol, E. Riseborough *et al.*, "Analysis of radar micro-Doppler signatures from experimental helicopter and human data," *Proc. Inst. Electr. Tech.—Radar Sonar Navig.*, vol. 1, no. 4, pp. 289–299, Aug. 2007.

[8] J. Li and H. Ling, "Application of adaptive chirplet representation for ISAR feature extraction from targets with rotating parts," *Proc. Inst. Electr. Eng.—Radar Sonar Navig.*, vol. 150, no. 4, pp. 284–291, Aug. 2003.

[9] Q. Zhang, T. S. Yeo, H. S. Tan *et al.*, "Imaging of a moving target with rotating parts based on the Hough transform," *IEEE Trans. Geosci. Remote Sens.*, vol. 46, no. 1, pp. 291–299, Jan. 2008.

[10] N. E. Huang, Z. Shen, S. R. Long *et al.*, "The empirical mode decomposition and the Hilbert spectrum for nonlinear and non-stationary time series analysis," *Proc. R. Soc. Lond. A, Math. Phys. Sci.*, vol. 454, no. 1971, pp. 903–995, Mar. 1998.

[11] N. E. Huang, M. C. Wu, S. R. Long *et al.*, "A confidence limit for the empirical mode decomposition and Hilbert spectral analysis," *Proc. R. Soc. Lond. A, Math. Phys. Sci.*, vol. 459, no. 2037, pp. 2317–2345, Sep. 2003.

[12] R. Deering and J. F. Kaiser, "The use of a masking signal to improve empirical mode decomposition," in *Proc. IEEE ICASSP*, Philadelphia, PA, Mar. 2005, vol. 4, pp. 485–488.

[13] T. Tanaka and D. P. Mandic, "Complex empirical mode decomposition," *IEEE Signal Process. Lett.*, vol. 14, no. 2, pp. 101–104, Feb. 2007.

[14] G. Rilling, P. Flandrin, P. Goncalves *et al.*, "Bivariate empirical mode decomposition," *IEEE Signal Process. Lett.*, vol. 14, no. 12, pp. 936–939, Dec. 2007.

[15] P. Flandrin, G. Rilling, and P. Goncalvés, "Empirical mode decomposition as a filter bank," *IEEE Signal Process. Lett.*, vol. 11, no. 2, pp. 112–114, Feb. 2004.

[16] H. Zhang and Q. Gai, "Research on properties of empirical mode decomposition method," in *Proc. 6th World Congr. Intell. Control Autom.*, Dalian, China, Jun. 21–23, 2006, pp. 10 001–10 004.

[17] D. R. Wehner, *High Resolution Radar*. Boston, MA: Artech House, 1995.

[18] Q. Wang, M. Xing, G. Lu *et al.*, "High-resolution three-dimensional radar imaging for rapidly spinning targets," *IEEE Trans. Geosci. Remote Sens.*, vol. 46, no. 1, pp. 22–30, Jan. 2008.

Xueru Bai was born in Shaanxi, China, in 1984. She received the B.S. degree from Xidian University, Xi'an, China, in 2006, where she is currently working toward the Ph.D. degree in signal and information processing in the National Key Laboratory for Radar Signal Processing. Her research interests are ISAR imaging and GMTI.

Mengdao Xing (S'00–A'03) was born in Zhejiang, China, in 1975. He received the B.S. and Ph.D. degrees from Xidian University, Xi'an, China, in 1997 and 2002, respectively.

He is currently a Professor with the National Key Laboratory for Radar Signal Processing, Xidian University. His research interests include radar imaging, target recognition, and over-the-horizon-radar signal processing.

Guangyue Lu received the Ph.D. degree from Xidian University, Xi'an, China, in 1999.

From September 2004 to August 2006, he was a Guest Researcher with the Signal and Systems Group, Uppsala University, Uppsala, Sweden. Since 2005, he has been a Professor with the Department of Telecommunications Engineering, Xi'an Institute of Posts and Telecommunications, Xi'an. His current research area is in radar imaging and signal processing in communication systems (such as orthogonal frequency-division multiplexing and code-division multiple access).

Feng Zhou was born in Henan, China, in 1980. He received the B.S. and Ph.D. degrees from Xidian University, Xi'an, China, in 2004 and 2007, respectively.

He is currently an Associate Professor with the National Key Laboratory for Radar Signal Processing, Xidian University. His research interests include radar imaging and interference suppression.

Zheng Bao (SM'88) was born in Jiangsu, China, in 1927. He received the B.S. degree from the Communication Engineering Institute of China (currently, Xidian University), Xi'an, China, in 1953.

He is currently a Professor with National Key Laboratory for Radar Signal Processing, Xidian University. He is also a member of the Chinese Academy of Sciences. He has authored or coauthored six books and published over 300 papers. His current research fields are in space–time adaptive processing, radar imaging (SAR/ISAR), automatic target recognition, over-the-horizon-radar signal processing, and passive coherent location.